MANAGER'S SUMMARY
ZCO-55, "Dross Minimization in the Galvanizing Bath"
Special Progress Report: September 14, 2009

The subject report describes work by a summer student to numerically model a bench top apparatus designed to simulate the flow of wiping gas and zinc in the downward direction along the sheet below the wiping knives, down to its point of contact with the galvanizing bath. This work and the results described in the report are judged as being very successful.

A detailed description of the mathematical modeling technique is given in the report, including development of the heat transfer, fluid flow and turbulence relationships from first principles together with a detailed treatment of boundary conditions. The practical results provided detailed information on heat losses and the nature of fluid flow patterns relevant to the cascading zinc surface below the wiping knives. Heat loss as a function of inlet flow rate is shown together with the flow of air at the zinc surface as the zinc cascades from the wiping knives down to the bath surface. The calculations also allow for calculation of the pressure on the falling zinc surface from the descending air adjacent to it. The model created will be very useful in interpreting the experimental results obtained with this apparatus, and in generalizing these results to industrial situations.

Distribution to:
GAP Sponsors of FA II and ZCO-55

Numerical Simulation of a Zinc Overflow Apparatus for the Study of Oxide Dross Formation

A. Navarra, F. Ilinca, F. Ajersch

September 14, 2009

Abstract

A novel experimental apparatus has been designed to investigate dross formation around a steel sheet, as it exits a galvanizing bath and is exposed to air knives. Prior to construction of the device, the k-ϵ model has been used in numerical simulations to estimate the convective heat losses; it was found that a heat supply of 10 kW is sufficient to run the physical experiments in the industrially relevant range of air flow rates. Also, it is observed that the numerical results can be extrapolated into higher flow ranges by scaling the dimensionless numerical results; however, the viscous interactions at the lower flow rates are more complicated, and cannot be extrapolated in the same way.

1 Introduction

1.1 Dross Formation during the Galvanization of Steel

Galvanization is a surface treatment whereby a corrosion-resistant zinc coating forms around a steel substrate. Galvanized strips are widely used in the automotive industry because they are readily paintable, deformable and weldable. Other applications include machine tools, household appliances and electric equipment.

In the galvanization process, steel strips are dipped into a molten zinc bath (450 to 480°C) containing 0.1 to 0.2 wt%Al [1, 2, 3]. The aluminum forms a thin layer of Fe_2Al_5 over the steel, thus blocking the formation of brittle Fe-Zn compounds. This inhibition layer is less than 1 μm thick, and is ultimately covered by the 10-15 μm Zn coating. The inhibition layer forms rapidly (0.1 to 0.3 s) but requires a uniform delivery of Al as the strip enters the bath [1]. If the inhibition layer is malformed, there will be Fe-Zn intermetallic inclusions, and the coating will not withstand the deformation processing.

A galvannealing process (which combines galvanization and annealing) uses 0.10 to 0.13 wt%Al in the bath; other operations may use up to 0.20 wt%Al [1, 2, 3, 4]. The low Al contents are prone to solid $FeZn_7$ precipitation, whereas the high Al contents are prone to solid Fe_2Al_5. Generally, all galvanizing baths have the potential for the precipitation of Fe-Zn-Al intermetallics and oxides, which culminate into a dross (solid suspension). Excessive dross formation interferes with Al transport, having a detrimental effect on the inhibition layer.

As the strip exits the bath with a given velocity (usually 0.5 to 2.0 m/s, ref), it is exposed to air knives which freeze the molten zinc onto the strip. Depending on the pressure of the blast and its proximity to the strip, a different quantity of zinc may be entrained, thus controlling the final thickness of the coating. But improper adjustment of the air knives can result in oxide dross formation, which weakens the coating.

The appropriate adjustment of the air knives depends on the bath composition, which is partly influenced by the composition of the strip. As the strip is continuously passed trough the bath, it saturates the zinc with iron and other alloying components. For example, if the strip contains chromium then it is likely that the bath will attain an equilibrium quantity of this metal; a negative consequence might be the entrainment of chromium oxide dross into the coating.

As new steel alloys are developed, it is an ongoing challenge to determine and enforce optimal air flow conditions for the exiting strip. Small quantities of alloying elements may interact synergistically with the zinc, iron and aluminum, thus bringing oxides and intermetallics into the coating. The final outcome is further complicated by the coupling of chemical, thermal and fluid mechanic phenomena. Therefore, it is imprudent to adapt real operations to new alloys without physical and numerical experimentation.

The present work is a series of numerical computations, in anticipation of physical experiments that will isolate and study oxide dross formation under controlled air currents. The isolation of this critical phenomenon will be accomplished with a novel apparatus, described in the following section. The experimental results will be relevant to the galvanization of new and existing steel alloys.

Several design parameters for the apparatus have not yet been finalized because their influence over the upcoming physical experiments is not sufficiently known. Some insight into the design will be provided by numerical simulation. It will be easier to numerically simulate several permutations of the apparatus than to modify the physical apparatus after its construction.

In this first set of computations, only the velocity and temperature patterns of the air will be considered. The molten zinc surfaces will be treated as static boundaries. The simplification is that the zinc surfaces are stationary, non-deformable and have the same stress response to tangential air flows as the solid boundaries. In future computations the zinc phase will be treated in more detail.

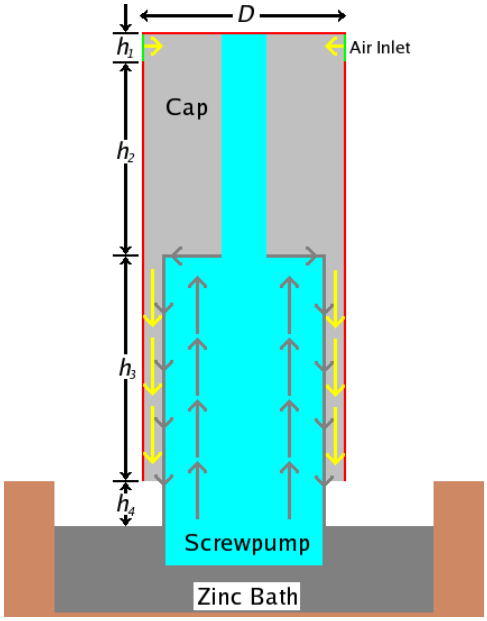

Figure 1: Diagram of Zinc Overflow Apparatus

1.2 Description of the Apparatus

The apparatus will consist of three main components (Figure 1). Firstly, there will be a cylindrical zinc bath. Secondly there will be a central tube, placed vertically in the bath, through which a screwpump will draw liquid zinc upward; as the zinc leaves the screwpump, it will fall along the outside of the tube, back into the bath. Thirdly there will be a steel cap above the bath, and overarching the central tube. The dimensions of the cap have not been finalized.

Air will be introduced near the top of the cap, along the outer diameter, and pointing radially inward. The air enters through equi-spaced perforations, so that the input velocity field $\mathbf{u}_i$ will be approximately uniform around the outer diameter, with typical magnitudes ranging from $u_i = 5$ m/s to $u_i = 15$ m/s. The only place for the air to escape will be along side the falling zinc, which is where chemical interactions will occur, resulting in oxide dross. The dross will accumulate along the side of the bath where it will be sampled and analyzed using LIBS (Laser-induced breakdown spectroscopy, [5]).

In the following simulation, the molten zinc will be treated as solid. Thus it is assumed that the shear forces induced by the flowing zinc do not affect air patterns, except perhaps in a small neighbourhood. In reality, the bath surface may behave quite differently from a flat surface, as the momentum from the incident air will cause waves and an overall concavity; secondly, the presence of dross will likely have an effect on the surface tension of the bath. The complex phenomena occurring on and below the surface of the bath may be the subject of future work, but are beyond the current scope.

This study focuses primarily on heat losses, as influenced by (i) the cap diameter and (ii) the inlet flow rate. Given that the available heat supply is roughly 10 kW, numerical simulations may be used to estimate an upper limit on the inlet flow rate, as a function of the cap diameter (and/or other design parameters). A numerical optimization of the cap dimensions will be possible after a prototype of the device is built, and

after several sets of experiments have been run. It will be possible to retrofit different caps, while the rest of the apparatus is unaltered.

The current study explores two different cap diameters, $D = 90$ mm and $D = 110$ mm, with input velocity fields u_i of 1, 2, 3, 5, 7, 10, 15 and 20 m/s. For the 90 mm cap, the u_i values correspond to flow rates of roughly 3, 6, 8, 14, 20, 28, 42 and 57 L/s. For the 110 mm cap, the u_i values correspond to flow rates of roughly 3, 7, 10, 17, 24, 35, 52, and 69 L/s. The other design parameters (Figure 1) are assigned as follows: $h_1 = 10$ mm, $h_2 = 90$ mm, $h_3 = 100$ mm and $h_4 = 20$ mm. Future computations can address these other parameters, and may form an addendum to this document.

1.3 Thermal Parameters, Density and Viscosity

Initially, the apparatus is at ambient temperature, 25°C. The temperature of the inlet air is set to 0°C, and that of the zinc surface is taken to be 420°C. The central shaft, rising from the pump, is also taken to be 420°C because of its direct contact with the molten zinc. The refractory bricks are assigned a temperature of 200°C, roughly the midpoint between the ambient and the zinc temperatures. Lastly the cap is treated as an insulator, because the heat conducted through the cap is expected to be negligible compared to the forced convection; this is implemented by setting the convective heat transfer coefficient to zero along the cap surface.

The current study assumes that the heat capacity c_p and thermal conductivity λ of air remain unchanged from their ambient values $c_p = 1000$ J/(kg·K) and $\lambda = 0.0257$ W/(m·K). It is notable that tabulated values [6] show an increase of 6% in c_p and 100% in λ, as temperature is increased from 25°C to 400°C. However, the hot zones are expected to be highly localized around the zinc surfaces, such that the ambient thermal properties will dominate. The density and viscosity are assumed constant $\rho = 1.205$ kg/m^3 and $\mu = 1.820 \cdot 10^{-5}$ Pa·s, which are also the ambient values.

The heat transfer coefficient over the free falling zinc is not well known, but previous measurements under similar circumstances give values of approximately $h = 50$ W/(m^2·K), according to preliminary readings taken under the supervision of Ajersch. For simplicity, the heat transfer coefficient between the air and the refractory is also taken as $h = 50$ W/(m^2·K), but this has negligible effect on the flow behaviour in and around the cap.

The upcoming experimental work will provide valuable feedback for future simulations, particularly with regards to the thermal parameters and the dross formation. These results will in turn be used to extrapolate operating conditions in industrial plants. The current work is only intended to give preliminary insight into thermal issues that may limit the experimental conditions.

2 Governing Equations

2.1 Heat Balance

The heat balance is given by:

$$\rho c_p \frac{DT}{Dt} = \nabla \cdot ((\lambda + \lambda_T)\nabla T) \tag{1}$$

where T denotes temperature. As described in Section 1.3, ρ, c_p and λ are the ambient density, specific heat and thermal conductivity of air. λ_T is the increase in thermal conductivity that is due to turbulence (see Section 2.3).

$\frac{D}{Dt}$ is the particular derivative which depends on the velocity field $\mathbf{u}$, as $\frac{D}{Dt} = (\frac{\partial}{\partial t} + \mathbf{u} \cdot \nabla)$. The second part of the particular derivative is the advection term, $\mathbf{u} \cdot \nabla$, which couples the heat transfer to the fluid motion. Turbulence gives an additional coupling because λ_T depends on $\mathbf{u}$, as described in Section 2.3.

Equation 1 states that heat diffuses into (out of) a small, moving volume of fluid, if it is exposed to a warmer (colder) medium, and that the rate diminishes as the temperature of the moving volume is equalized with its surroundings. The motion of the fluid particle is addressed by the advection term in the particular derivative. The rate of heat accumulation ($\frac{D(\rho c_p T)}{Dt}$) is expressed on a per-unit-volume basis, because Equation 1 is the result of a limiting process in which the size of the volume (and hence the net heat content) of the fluid goes to zero.

2.2 Incompressible Navier-Stokes Equations

Having assumed constant air density ρ, the incompressible Navier-Stokes equations describe the velocity field $\mathbf{u}$ and the pressure p:

$$\rho \frac{D\mathbf{u}}{Dt} = -\nabla p + \nabla \cdot (2(\mu + \mu_T)\dot{\gamma}) \tag{2}$$

$$\nabla \cdot \mathbf{u} = 0 \tag{3}$$

where $\dot{\gamma}(\mathbf{u}) = (\frac{\nabla \mathbf{u} + \nabla \mathbf{u}^T}{2})$ is the strain-rate tensor. μ_T is the increase in viscosity due to turbulence, which depends on the velocity field $\mathbf{u}$ (see Section 2.3). For the following computations, p is the gauge pressure with respect to atmospheric conditions, 101.3 kPa.

Equation 2 is an extension of Newton's second law: the rate of change of momentum within a small moving volume is equal to the sum forces acting upon it. These forces give the inwardly compressive pressure term ($-\nabla p$), and the viscous shearing term ($\nabla \cdot (2(\mu + \mu_T)\dot{\gamma})$. As with the heat balance (Equation 1), the momentum equation (Equation 2) is the result of a limiting process over a small volume, therefore the momentum change ($\frac{D(\rho \mathbf{u})}{Dt}$) is expressed on a per-unit-volume basis.

Equation 3 may be derived from the condition that the density is constant ($\partial \rho = 0$), that mass is conserved, and that mass is continuously distributed in space. Therefore Equation 2 is commonly understood as the mass-continuity condition for incompressible fluids, or simply the "incompressibility condition".

2.3 Turbulence

Turbulence is incorporated into the momentum and heat balances through the turbulent viscosity μ_T and the turbulent heat conductivity λ_T, which are given according to the standard k-ϵ model [1, 2, 3, 4]:

$$\mu_T = C_\mu \rho \frac{k^2}{\epsilon} \tag{4}$$

$$\lambda_T = \left(\frac{C_\mu \rho c_p}{\mathrm{Pr}_T} \right) \frac{k^2}{\epsilon} \tag{5}$$

Both μ_T and λ_T are proportional to the ratio $(\frac{k^2}{\epsilon})$, where k is the turbulent kinetic energy (in $\mathrm{m}^2/\mathrm{s}^2$) and ϵ is the turbulent dissipation (in $\mathrm{m}^2/\mathrm{s}^3$). $C_\mu = 0.09$ is a model constant, and Pr_T is the turbulent Prandtl number taken to be unity $\mathrm{Pr}_T = 1$. Once a value of μ_T is obtained, λ_T may be calculated simply as

$$\lambda_T = \frac{c_p \mu_T}{\mathrm{Pr}_T} \tag{6}$$

The turbulent viscosity μ_T is computed simultaneously with $k - \epsilon$ according to:

$$\rho \frac{Dk}{Dt} = \nabla \cdot \left[\left(\mu + \frac{\mu_T}{\sigma_k} \right) \nabla k \right] + P - \rho\epsilon \tag{7}$$

$$\rho \frac{D\epsilon}{Dt} = \nabla \cdot \left[\left(\mu + \frac{\mu_T}{\sigma_\epsilon} \right) \nabla k \right] + C_{\epsilon 1} \frac{\epsilon}{k} P - C_{\epsilon 2} \rho \frac{\epsilon^2}{k} \tag{8}$$

where $\sigma_k = 1.0$, $\sigma_\epsilon = 1.3$, $C_{\epsilon 1} = 1.44$ and $C_{\epsilon 2} = 1.92$ are model constants, and P is the shear production term, given by:

$$P = \mu_T \left[\nabla \mathbf{u} : (\nabla \mathbf{u} + \nabla \mathbf{u}^T) \right] \tag{9}$$

where the dyadic product is defined as $A : B = \sum_{i=1}^{m} \sum_{j=1}^{n} a_{ij} b_{ij}$ for two $(m \times n)$ matrices A and B.

Equation 7 is a balance of the turbulent kinetic energy (TKE), and is analogous to the heat and momentum balances, Equations 1 and 3, respectively. The energy available to form turbulent eddies is that which is deducted by viscous action from the global stream; therefore the transport of turbulent kinetic energy into a small moving volume is related to μ. In Equation 7, μ acts like a conductivity coefficient, with an additional feedback expressed by μ_T/σ_k.

Aside from the external viscous contribution of the TKE, there is also local production due to the shearing action of local eddies, as described by P. This is dampened by the rightmost term in Equation 7, $-\rho\epsilon$. Through this term, ϵ may be interpreted as the quantity of "turbulence dissipator" per unit mass of air; thus, $\rho\epsilon$ is the quantity on a per-unit-volume basis.

Following this interpretation of ϵ, Equation 8 is the balance of the dissipator in a small volume of fluid that is in motion. Again, μ acts as a conductivity that introduces dissipator from global streams, with an additional feedback μ_T/σ_ϵ. The local production/consumption of dissipator is expressed on a per-unit-volume basis by the final two terms in Equation 8.

Turbulence, as described by the standard $k-\epsilon$ model, is dependent on the velocity field via the particular derivative (Equations 7 and 8) and the shear production term (Equation 9). A more complete version of this model would also include a perturbation on P due to buoyancy effects (see [1], for example), which would add an additional coupling with the heat balance (Equation 3). However, this effect is negligible in the current study.

A computational difficulty arises in the solution of the turbulence equations (Equations 7 and 8) because k occurs in the denominator of the final two terms in Equation 8, and because the formula for μ_T contains ϵ in the denominator. Errors in these denominators are magnified when k and ϵ are small. These errors cause a breakdown in the solution algorithm especially when k and ϵ are misrepresented as negative numbers. To enhance computational stability, the computation is done with respect to the logarithms:

$$\mathcal{K} = \ln(k) \qquad \mathcal{E} = \ln(\epsilon) \tag{10}$$

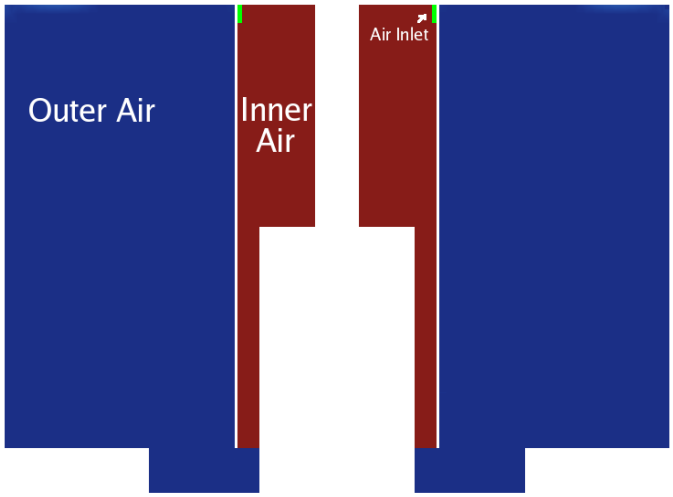

Figure 2: Diagram of Simulation Zone

The computation of $\mathcal{K}$ and $\mathcal{E}$ guarantees that k and ϵ remain positive throughout the computations.

The turbulence equations are rewritten as

$$\rho\frac{D\mathcal{K}}{Dt} = \nabla\cdot\left[\left(\mu+\frac{\mu_T}{\sigma_k}\right)\nabla\mathcal{K}\right] + \left(\mu+\frac{\mu_T}{\sigma_k}\right)(\nabla\mathcal{K}^T\nabla\mathcal{K}) + e^{-\mathcal{K}}P - \rho e^{\mathcal{E}-\mathcal{K}} \tag{11}$$

$$\rho\frac{D\mathcal{E}}{Dt} = \nabla\cdot\left[\left(\mu+\frac{\mu_T}{\sigma_\epsilon}\right)\nabla\mathcal{E}\right] + \left(\mu+\frac{\mu_T}{\sigma_\epsilon}\right)(\nabla\epsilon^T\nabla\epsilon) + C_{\epsilon 1}e^{-\mathcal{K}}P - C_{\epsilon 2}\rho e^{\mathcal{E}-\mathcal{K}} \tag{12}$$

where the turbulent viscosity μ_T is calculated as

$$\mu_T = \rho C_\mu e^{2\mathcal{K}-\mathcal{E}} \tag{13}$$

and $\lambda_T = \frac{c_p\mu_T}{\mathrm{Pr}_T}$, as before.

2.4 Boundary Conditions

As depicted in Figure 2, the simulation region includes a region surrounding the cap (blue), in addition to the interior of the cap (red). The thickness of the cap is represented by the thin white strips separating the outer and inner air, on either side of the figure. As the air is introduced through the green region of Figure 2, it is forced downward. Once it exits the cap, it disperses outward and upward.

Through the course of the simulations, it was found that the solutions were more stable if the perimeter of the outer air region was treated as an insolating wall, rather than being open. Therefore, the only way for the air to leave the system is along the top of the outer air region. This does not adversely affect the validity of the results, because the perimeter of the outer air region is sufficiently far from the bath.

The boundary of the simulation zone Γ is partitioned into three mutually disjoint regions $\Gamma = \Gamma_i \cup \Gamma_o \cup \Gamma_w$, such that Γ_i is the inlet at the top of the inner cap region, Γ_o is the top surface of the outer region and Γ_w

refers to every other surface, including the perimeter of the outer air, the cap surface, the refractory surface and the zinc.

As described in Section 1.2, the air entering from Γ_i has constant temperature $T_i = 0°\text{C}$, and conforms to the following flow condition:

$$\mathbf{u}_i = -u_i \hat{\mathbf{r}} \tag{14}$$

where u_i is the inlet flow rate, and $\hat{\mathbf{r}}$ is the unit normal in the radial direction. The inflowing air carries the following turbulence kinetic energy:

$$k_i = 0.04 u_i^2 \tag{15}$$

Within a thin layer of the inlet zone, the dissipation follows the equation

$$\epsilon_i = 0.0032 \frac{u_i^3}{y} \tag{16}$$

where y is the distance form the nearest wall surface Γ_w.

Following the incompressibility condition (Equation 3), independent flow conditions cannot be placed on Γ_o. Essentially, the air that enters through Γ_i must leave through Γ_o, otherwise the incompressibility condition is violated. Also, it can be assumed that the transport of heat, TKE and dissipation is dominated by advection at the outlet, so the specification of T, TKE and ϵ are not relevant.

Now let y be the distance separating Γ_w from a given point in the simulation zone. Again, this point is part of the boundary if $y < 0.5$ mm. The points within the boundary layer satisfy a combination of tangential and normal conditions on the flow variables $(\mathbf{u}, p)$:

$$\left.\begin{array}{rcl} [2(\mu + \mu_T)\dot{\gamma} \cdot \mathbf{n} - p\mathbf{u}] \cdot \hat{\mathbf{t}}_i & = & \tau_w \cdot \hat{\mathbf{t}}_i \\ \mathbf{u} \cdot \hat{\mathbf{n}} & = & 0 \end{array}\right\} \text{on } \Gamma_w \tag{17}$$

The unit vectors $\hat{\mathbf{t}}_i$ span the tangential plane at a given point on Γ_w, while $\hat{\mathbf{n}}$ is normal to the plane.

The shear stress τ_w is computed from the wall function,

$$\tau_w = -\frac{\rho C_\mu^{1/4} k_w^{1/2}}{U^+} \mathbf{u} \tag{18}$$

where

$$U^+ = \begin{cases} y^+ & \text{when } y < y_c \\ \frac{1}{\kappa} \ln(E y^+) & \text{when } y \geq y_c \end{cases} \tag{19}$$

$$y^+ = \frac{\rho C_\mu^{1/4} k_w^{1/2} y}{\mu} \tag{20}$$

$\kappa = 0.41$ is the Von Karman constant, $E = 9.0$ a roughness parameter, y is the distance from the wall. y_c satisfies $y_c = \frac{1}{\kappa} \ln(E y^+)$, which ensures the continuity of Equation 19.

k_w is the TKE calculated at the wall. The model assumes that the wall is an insulator to turbulence, so that the TKE in the boundary k_w satisfies:

$$\nabla k_w \cdot \hat{\mathbf{n}} = 0 \tag{21}$$

from which k_w is computed implicitly. The dissipation in the boundary, is then calculated according to:

$$\epsilon_w = \frac{C_\mu^{3/4} k_w^{3/2}}{\kappa y} \tag{22}$$

The heat transfer within the boundary layer is described by:

$$q_w = \frac{h_T h}{h_T + h}(T_w - T) \tag{23}$$

where q_w is the heat flux from the wall into the simulation zone, defined by

$$q_w = -(\lambda + \lambda_T)\nabla T \cdot \hat{\mathbf{n}} \tag{24}$$

T_w and h are the temperature of the given wall region and the heat transfer coefficient, as described by Section 1.3. h_T represents an additional heat transfer acting in series with the nominal convection, and is due to turbulence:

$$h_T = \frac{\rho c_p C_\mu^{1/4} k_w^{1/2}}{T^+} \tag{25}$$

where T^+ is a function of y^+, as described by [7]

$$T^+ = \begin{cases} \Pr\, y^+ & y^+ < y_1^+ \\ a_2 - \frac{\Pr_T}{2a_1(y^+)^2} & y_1^+ \le y^+ < y_2^+ \\ \frac{\Pr_T}{K}\ln(y^+) + \beta & y_2^+ \le y^+ \end{cases} \tag{26}$$

Equation 26 includes the following definitions:

$$y_1+ = \frac{10}{\Pr^{1/3}} \qquad y_2+ = \frac{K^{1/2}}{a_1}$$

$$a_1 = 10^{-3}\Pr_T \qquad a_2 = 15\Pr^{2/3}$$

$$\beta = a_2 - \frac{\Pr_T}{2K}\left[1 + \ln(K/a_1)\right]$$

where $\Pr = \left(\frac{c_p \mu}{\lambda}\right)$ is the Prandtl number.

This section has described the boundary conditions that were used to simulate the air flow, and heat transport. The procedure by which an initial solution ($t = 0$ seconds) was obtained is described in Section 3.3.

3 Computational Methodology

3.1 Descretization

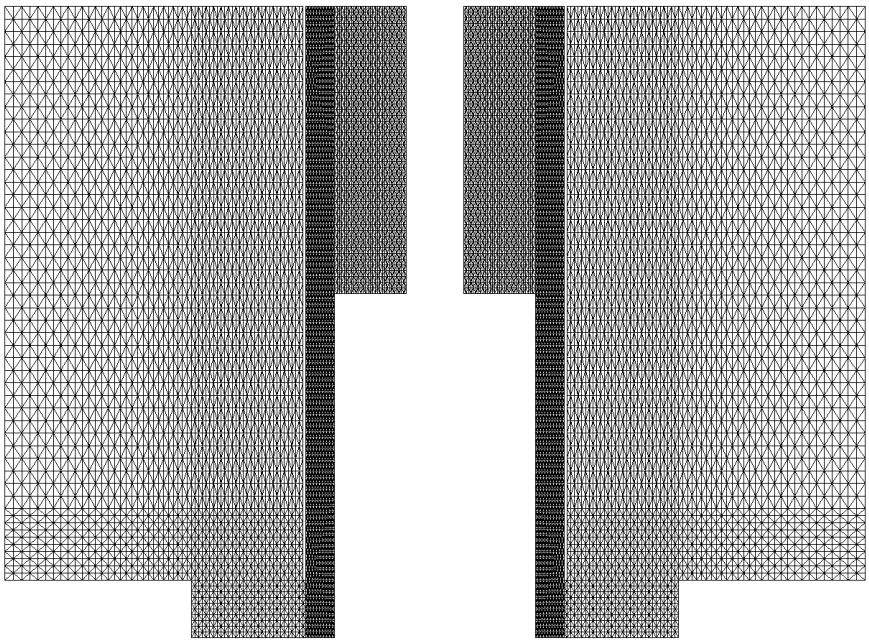

Figure 3: Descretization for $D = 90$ mm

As depicted by Figures 3 and 4, the simulation zones for the 90 mm diameter cap and the 110 mm diameter cap, are each represented by a structured grid. These grids were built to provide more precise calculations in the regions having larger velocity gradients. The most detailed region is the area surrounding the falling zinc wall.

Moving radially outward away from the cap, the grid elements become increasingly larger, as the velocity gradients are expected to be smaller. The regions immediately above the refractory surface is represented with more detail than the higher regions that are higher up.

Figures 3 and 4 show a single slice of the simulation zone. In fact, the entire zone consists of 36 such slides, each having a 10° separation. The elements are tetrahedral, with the vertices inhabiting the nodes of the structured grid. The unknown quantities $\{T, \mathbf{u}, p, \mathcal{K}, \mathcal{E}\}$ are taken to be a linear approximation to the solution of the differential equations described in the previous sections.

For the 90 mm cap, the descretization consisted of 291280 nodes and 1402000 elements. For the 110 mm cap, the descretization consisted had 323680 nodes and 1562000 elements.

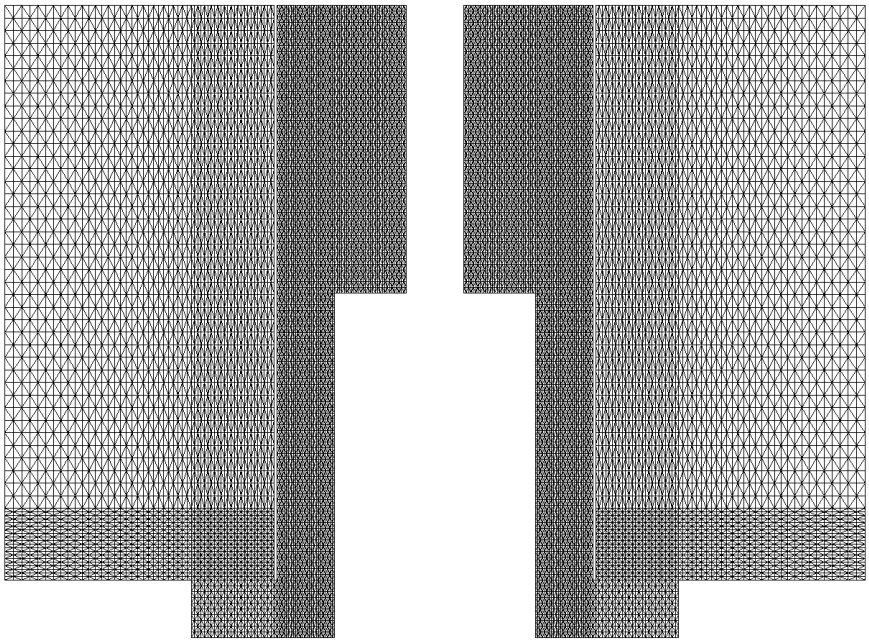

Figure 4: Descretization for $D = 110$ mm

3.2 Nondimensionalization

The computations were performed with respect to nondimensional parameters, denoted with a tilda sign. For instance, the nondimensional density was taken to be $\tilde{\rho} = \frac{\rho}{\rho_o} = 1$, in all of the simulations. Likewise, the specific heat is normalized to $\tilde{c_p} = \frac{c_p}{c_{p,o}} = 1$; the scaling factors ρ_o and $c_{p,o}$ were taken to be density and specific heat of ambient air, for simplicity. Generally, the nondimensional approach provides insight into the dominant phenomena affecting a process, and the simplifications that can be applied to a given model [8].

The viscosity μ and thermal conductivity λ of air were scaled as a function of the inlet velocity u_i, as was the heat transfer coefficient h between the air and the convection surfaces.

$$\tilde{\mu} = \frac{\mu}{\mu_o} = \frac{\mu}{\rho_o l_o u_i} \tag{27}$$

$$\tilde{\lambda} = \frac{\lambda}{\lambda_o} = \frac{\lambda}{\rho_o c_{p,o} l_o u_i} \tag{28}$$

$$\tilde{h} = \frac{h}{h_o} = \frac{h}{\rho_o c_{p,o} u_i} \tag{29}$$

where l_o is the characteristic length of the system, taken to be 0.001 m.

The dimensionless inlet pressure was normalized ($\tilde{u_i} = \frac{u_i}{u_i} = 1$) for all the simulations. As will be explained in the following section, this gives a beneficial similarity between the initial solutions for the different simulations. Due to this approach, the changes in inlet velocity were implemented as changes in $\tilde{\mu}$, $\tilde{\lambda}$ and $\tilde{h}$, even though $\tilde{u_i}$ remains unchanged (see Table 1).

$u_i(m/s)$	$\tilde{u_i}$	$\tilde{\mu}$	$\tilde{\lambda}$	$\tilde{h}$
1	1	0.0151	0.0213	0.0415
2	1	0.00755	0.0107	0.0208
3	1	0.00504	0.00711	0.0138
5	1	0.00302	0.00427	0.00830
7	1	0.00216	0.00305	0.00593
10	1	0.00151	0.00213	0.00415
15	1	0.00101	0.00142	0.00277
20	1	0.000755	0.00107	0.00207

The final simulations were performed over 100 time-steps, each representing a dimensionless quantity of time $\tilde{\Delta}t = 1$. However, the scaling of the time-step varied as a function of u_i,

$$\Delta t = t_o \cdot (\tilde{\Delta}t) = \left(\frac{l_o}{u_i}\right)\tilde{\Delta}t \tag{30}$$

where Δt is the duration of the time-step, measured in seconds.

The computational outputs are nondimensional, except for the temperature field which is computed directly in °C. The other results must multiplied by the appropriate scaling factor before they can be compared to experimental measurements. The computed flow variables are $\tilde{\mathbf{u}}$, scaled as

$$\mathbf{u} = u_i\tilde{\mathbf{u}} \tag{31}$$

and $\tilde{p}$, scaled as

$$p = p_o\tilde{p} = \rho_o u_i^2\tilde{p} \tag{32}$$

Recall that p is the gauge pressure with respect to atmospheric pressure p_{atm}. In order to convert the computational result into absolute pressure, the following formula may be employed:

$$p_{absolute} = \rho_o u_i^2\tilde{p} + p_{atm}$$

But in this study, it is more practical to consider the gauge pressure, so Equation 32 suffices.

The turbulence parameters are scaled as

$$k = k_o\tilde{k} = u_i^2\tilde{k} \tag{33}$$

$$\epsilon = \epsilon_o\tilde{\epsilon} = \left(\frac{u_i^3}{l_o}\right)\tilde{\epsilon} \tag{34}$$

This may be expressed with respect to the logarithmic forms:

$$k = u_i^2 \exp\left(\tilde{\mathcal{K}}\right) \tag{35}$$

$$\epsilon = \left(\frac{u_i^3}{l_o}\right)\exp\left(\tilde{\mathcal{E}}\right) \tag{36}$$

where $\tilde{\mathcal{K}} = \ln\left(\frac{k}{k_o}\right)$ and $\tilde{\mathcal{E}} = \ln\left(\frac{\epsilon}{\epsilon_o}\right)$ are computed from Equations 11-13.

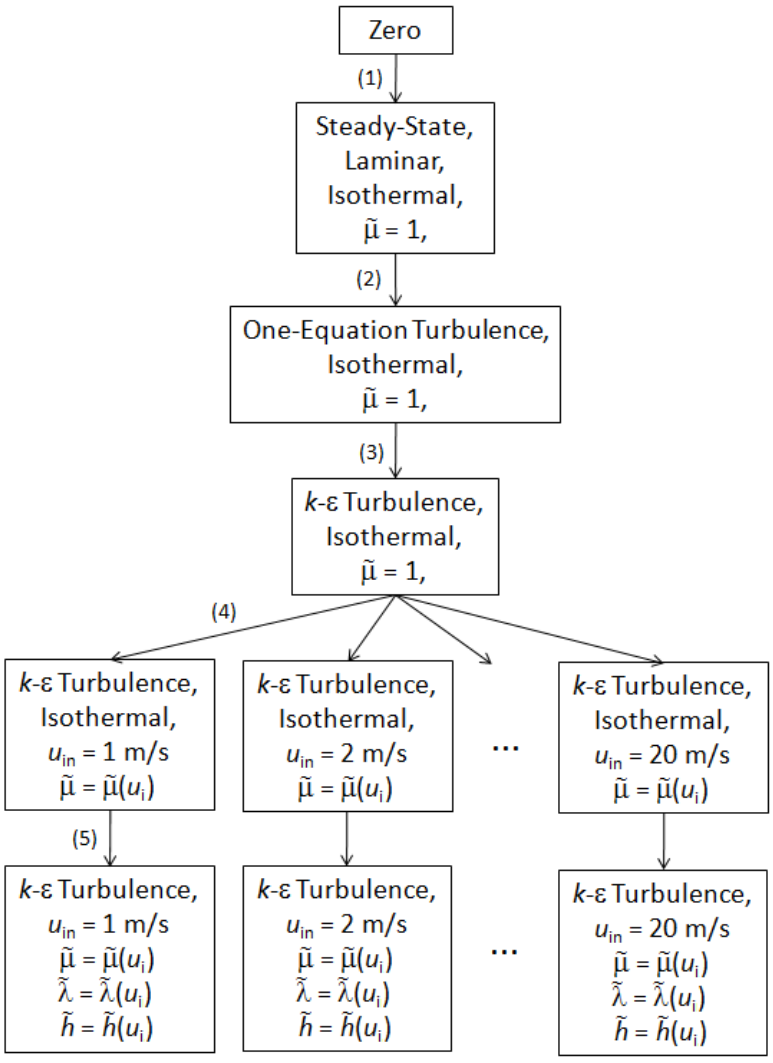

Figure 5: Computation Sequence

3.3 Generation of Initial Conditions

Figure 5 describes the computation sequence used to obtain the final set of solutions. Changes in inlet velocity u_i are only considered in the final two stages. In penultimate stage, the changes in u_i are implemented in the nondimensional viscosity $\tilde{\mu}$. In the final stage, the changes in u_i are implemented in $\tilde{\mu}$ as well as the thermal parameters $\tilde{\lambda}$ and $\tilde{h}$ (See Table 1). Temperature variations are only considered in the final stage.

Stage 1 assumes an initial condition over the entire simulation zone that $\tilde{\mathbf{u}} = 0$ and $p = 0$. In order to obtain a solution for the flow variables relatively quickly, time-variations and turbulence are dropped ($\frac{\partial}{\partial t} = \mu_T = 0$). This gives a steady-state laminar solution, that does not require time-step iterations.

The result of this computation is the initial solution for a simplified turbulence model, which is due to Prandtl [9],

$$\rho \frac{Dk}{Dt} = \nabla \cdot \left[\left(\mu + \frac{\mu_T}{\sigma_k} \right) \nabla k \right] + P - \rho\epsilon \tag{37}$$

$$\epsilon = \frac{C_\mu^{3/4} k^{3/2}}{\kappa y} \tag{38}$$

The transport equation for turbulent kinetic energy (Equation 37) is identical to that of the standard $k-\epsilon$ model (Equation 7), but the transport equation for ϵ (Equation 9) has been replaced by a closed form (Equation 38), which can be directly substituted into Equation 37. This turbulence model can therefore be expressed with a single differential equation, hence it is called the "one-equation" model. In the current study, the one-equation model is applied for ten nondimensional time-steps of length $\tilde{\Delta}t = 1$.

Stage 3 applies the standard $k-\epsilon$ model to the results of the simplified one-equation model, for a hundred time-step iterations of $\tilde{\Delta}t = 1$. The rough similarity between the solution to the one-equation model and the $k-\epsilon$ model is essential to the convergence of the first few iterations of Stage 3. Thus, the one-equation model is a computational bridge between the laminar steady-state solution and the standard $k-\epsilon$ solution.

Stage 3 provides a preliminary solution that is close to the solutions of Stage 4, which assists the convergence. The only change that is brought on by Stage 4 is the variation in dimensionless viscosity, as per Table 1. Of course, these minor changes in $\tilde{\mu}$ correspond to significant changes in u_i, which can be recovered by appropriately scaling. Thus, the nondimensional approach provides a tremendous saving in computation, because the same preliminary solution can be reused for all test values for u_i. For each of the different u_i values, Stage 4 applies 100 time-step iterations of $\tilde{\Delta}t = 1$.

Finally in Stage 5, temperature variations are introduced. Technically speaking, the initial condition for the final simulation is the flow pattern set forth by blowing away air that is initially at $T = 25°\text{C}$, and is sitting over a bath and refractories that are also at $T = 25°\text{C}$. In the first instant of the simulation, the inlet air is cooled to $T = 0°\text{C}$, the refractories are warmed to $T = 200°\text{C}$ and the zinc surfaces are warmed to $T = 420°\text{C}$.

3.4 Application of the FEM Method

The steady-state laminar solution (Stage 1) is obtained through the simple application of Picard and Newton iterations [10], and does not require time-step loops, nor does it consider turbulence. These iterations transform the zero solution into piece-wise linear functions that best approximate the solution of the differential equations. The Picard iterations are applied first because they have a large radius of convergence; once the solution has made some progress, Newton iterations are applied because they ultimately have a faster rate of convergence.

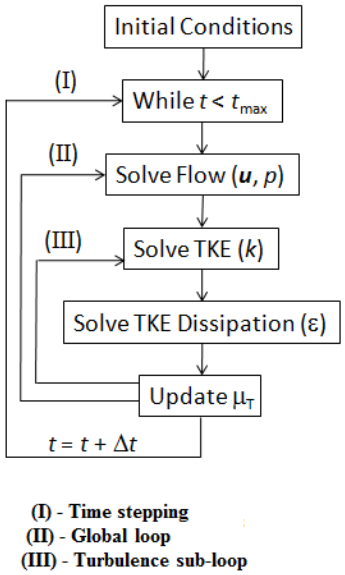

Figure 6: Algorithm for isothermal transient problems

The strategy employed for Stages 2, 3 and 4 is depicted in Figure 6. Loop I controls the evolution of the system in time. Within each time step, the global loop is applied to solve the Navier-Stokes equations (Equation 2 and Equation 3) using the streamline-upwind Petrov-Galerkin (SUPG) method [4, 11], assuming a constant value for the turbulent viscosity μ_T. The SUPG method includes stabilization terms that smoothen the solutions to convection-dominated flows. The global loop is cycled three times for every time-step, which ensures accurate approximations over time.

Within the global loop is the turbulence sub-loop, in which the updated flow variables $(\mathbf{u}, p)$ are taken as constant to solve the turbulence equations via Newton iterations. The sub-loop is applied three times within each passage of the global loop. As depicted in Figure 6, μ_T is updated at the end of the sub-loop, thus μ_T is updated three times before the flow variables are finally updated. By devoting more computation time to the sub-loop, the convergence of the global loop is accelerated.

To obtain the temperature-dependent solutions (Stage 5), the turbulent conductivity λ_T is updated after the turbulence sub-loop. An approximate solution to the heat balance (Equation 1) is then obtained using Newton iterations; this gives the temperature distribution throughout the simulation zone.

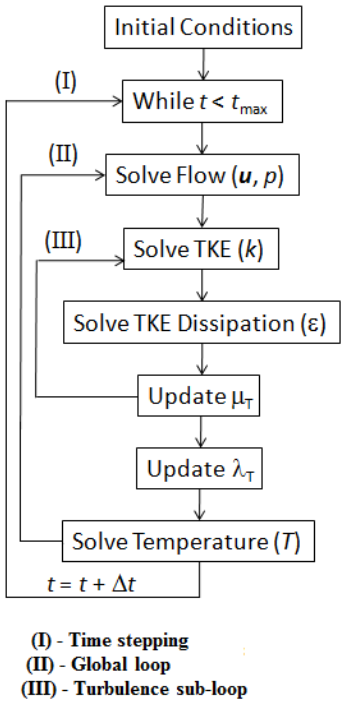

Figure 7: Algorithm for temperature-dependent transient problems

4 Results

4.1 Heat Losses

For both cap diameters, the overall temperature distributions are essentially unchanged for inlet flow rates that are above 10 m/s (Figure 8). Therefore, the heat losses scale directly with the flow rate, when $u_i \geq 10$ m/s. Figure 9 demonstrates that the trend becomes almost linear for both diameters.

By extending the linear trends in Figure 9, it is estimated that the experimental heat supply is sufficient for volumetric flow rates up to 280 L/s for $D = 90$mm, and up to 720 L/s for $D = 110$mm. This is far beyond the experimental interest. Therefore, the experiments are likely to be successful, unless the underlying simplifications described in Section 1.3 cause grave misrepresentations.

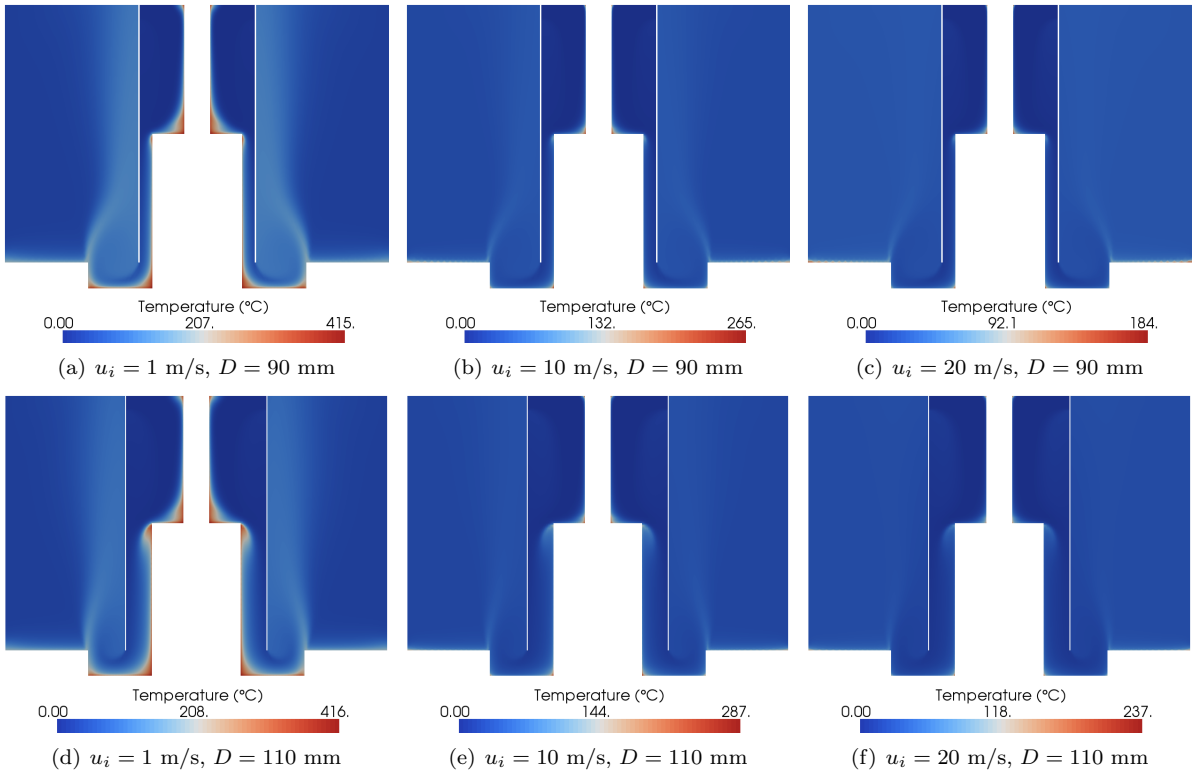

(a) $u_i = 1$ m/s, $D = 90$ mm (b) $u_i = 10$ m/s, $D = 90$ mm (c) $u_i = 20$ m/s, $D = 90$ mm

(d) $u_i = 1$ m/s, $D = 110$ mm (e) $u_i = 10$ m/s, $D = 110$ mm (f) $u_i = 20$ m/s, $D = 110$ mm

Figure 8: Temperature distribution as a function of input velocity u_i, and cap diameter D

For a given flow rate, the 90 mm diameter cap loses more heat than the 110 mm, essentially because the outgoing air is more concentrated around the falling zinc. For the 90 mm diameter cap, the annular opening has a smaller cross-sectional area, thus a higher velocity for a given flow rate. Most importantly, there is a higher velocity in the air immediately surrounding the falling zinc, which is where the heat exchange occurs.

The convective heat loss is coupled to the oxygen deposition, because both these phenomena depend on the velocity field surrounding the zinc bath. To maximize the oxide dross formation, the cap should be as tight as it can be, without causing excessive heat loss. An appropriate diameter size may be determined by

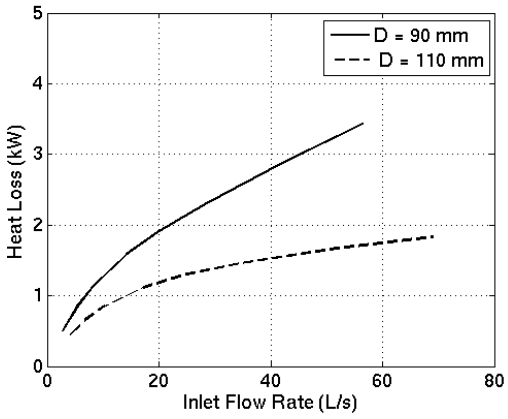

Figure 9: Heat loss as a function of inlet flow rate and cap diameter

setting an upper bound on the flow rate that will be used, and on the allowable heat loss.

The most critical thermal parameter, which may need to be determined experimentally, is the heat transfer coefficient occurring between the falling zinc and the surrounding air. Future simulations may be performed to demonstrate the effect that this coefficient will have over the upcoming experiments.

4.2 Flow Variables

Figure 10 shows the direction taken by the air flow, as it enters from the inlet and eventually leaves through the top of the outer air region. Figure 11 shows the magnitude of of the velocity field. The largest velocities occur at the top of the zinc fall.

For the large inlet velocities $u_i \geq 10$, rules-of-thumb can be established to estimate the maximum velocity field.

$$u_{\max} \approx 1.58 \cdot u_i \qquad \text{if } u_i \geq 10 \text{ m/s} \tag{39}$$

when $D = 90$ mm, and

$$u_{\max} \approx 1.28 \cdot u_i \qquad \text{if } u_i \geq 10 \text{ m/s} \tag{40}$$

when $D = 110$ mm. The balance between turbulent viscosity μ_T and laminar viscosity μ is different at the lower velocities, so these approximations do not apply when $u_i < 10$.

Figures 12 and 13 show the tangential velocity profile along the falling zinc surface, where most of the reactions are expected to take place. The left side of the plots correspond to bottom of the zinc fall (i.e. the bath), and the right side corresponds to the top of the fall. The line style convention presented in Figure 12a, to distinguish between the different inlet velocities u_i is used throughout Figures 12, 13, 15 and 16.

The z-component of the velocity is generally negative because the air is being forced out the bottom of the cap. However, there is a region close to the top of the fall where the velocity becomes positive as the air is pulled into a turbulent region; this is observed in the right side of Figures 12a and 13a.

Rules-of-thumb may be useful for modeling the reactions that occur as the zinc falls. For instance, the velocity at the midpoint of the fall can estimated with

$$u_{\text{fall}} \approx -0.96 \cdot u_i \qquad \text{if } u_i \geq 10 \text{ m/s} \tag{41}$$

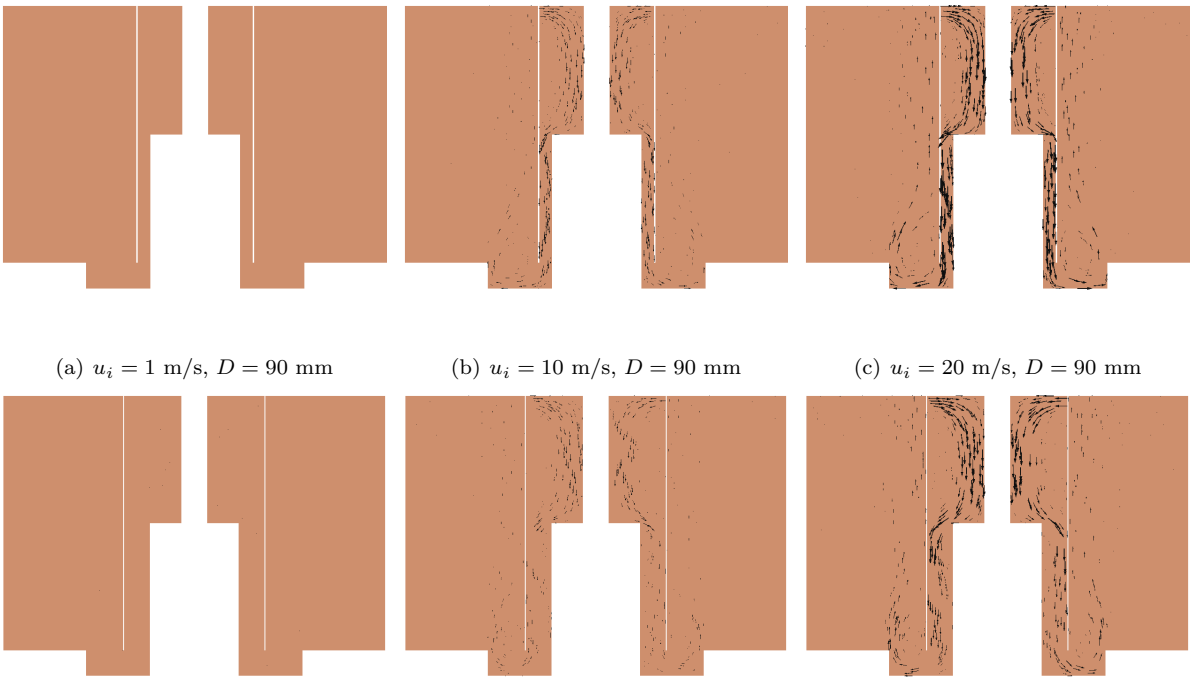

(a) $u_i = 1$ m/s, $D = 90$ mm (b) $u_i = 10$ m/s, $D = 90$ mm (c) $u_i = 20$ m/s, $D = 90$ mm

(d) $u_i = 1$ m/s, $D = 110$ mm (e) $u_i = 10$ m/s, $D = 110$ mm (f) $u_i = 20$ m/s, $D = 110$ mm

Figure 10: Velocity vector diagrams as a function of input velocity u_i, and cap diameter D

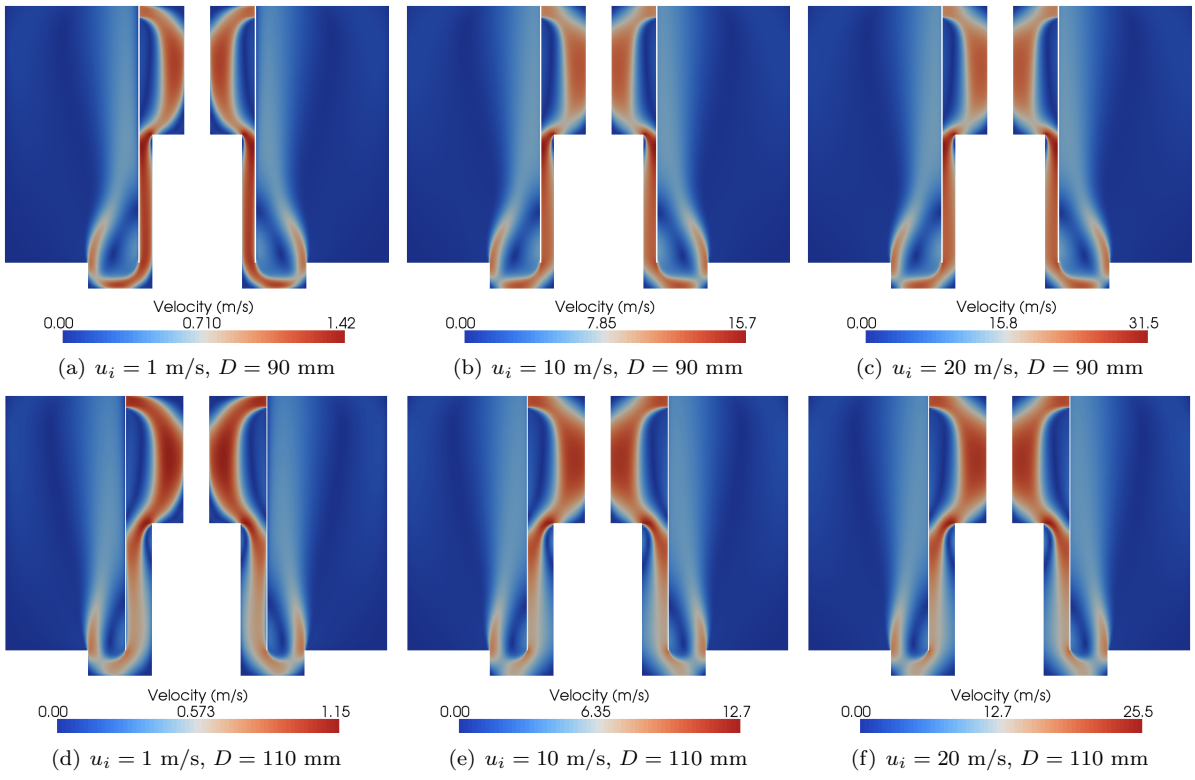

(a) $u_i = 1$ m/s, $D = 90$ mm (b) $u_i = 10$ m/s, $D = 90$ mm (c) $u_i = 20$ m/s, $D = 90$ mm

(d) $u_i = 1$ m/s, $D = 110$ mm (e) $u_i = 10$ m/s, $D = 110$ mm (f) $u_i = 20$ m/s, $D = 110$ mm

Figure 11: Velocity magnitude as a function of input velocity u_i, and cap diameter D

which gives the z-component along the falling zinc when $D = 90$ mm, and

$$u_{\text{fall}} \approx -0.30 \cdot u_i \qquad \text{if } u_i \geq 10 \text{ m/s} \tag{42}$$

which gives the z-component along the falling zinc when $D = 110$ mm. Eventually, it may be helpful to fit a general curve that would give the air velocity all along the falling zinc surface.

It can be observed from the dimensionless plots (Figure 12b and 13b) that there is a varying balance between the laminar and turbulent phenomena when the inlet velocities become small. The dimensionless curves for u_i <10 m/s are dispersed, whereas those for u_i ≥10 m/s are virtually superimposed.

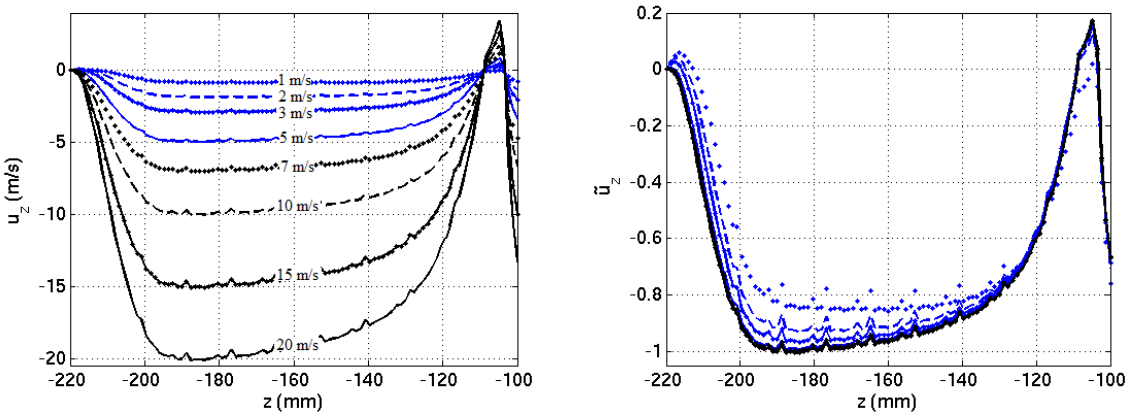

(a) Dimensional (b) Nondimensional

Figure 12: Vertical velocity along the falling zinc surface, with cap diameter $D = 90$mm

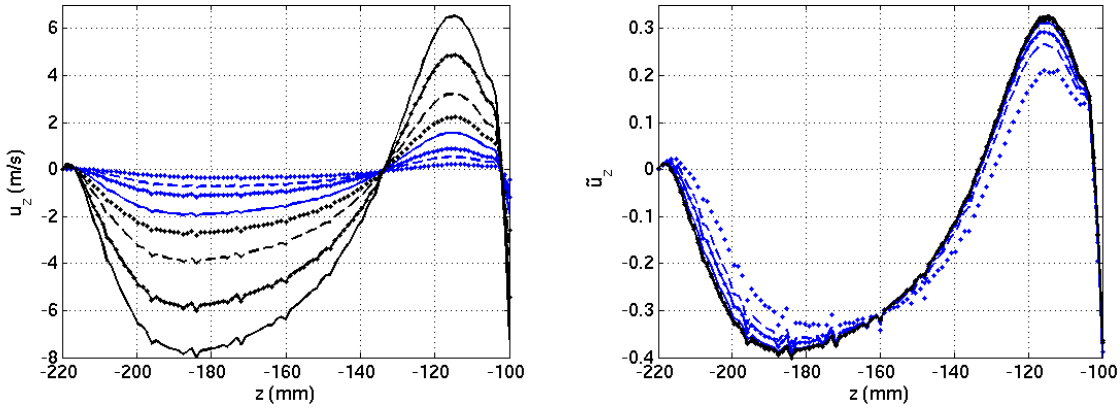

(a) Dimensional (b) Nondimensional

Figure 13: Vertical velocity along the falling zinc surface, with cap diameter $D = 110$mm

Figure 14 is a display of the gauge pressure distribution. For both $D = 90$mm and $D = 110$mm, an unalleviated pressure is observed surrounding the screwpump assembly and the central shaft. The following estimates can be established for the cases when $u_i \geq 10$,

$$p_{\max} \approx 0.00217 \cdot \rho u_i^2 \qquad \text{if } u_i \geq 10 \text{ m/s} \tag{43}$$

when $D = 90$ mm, and

$$p_{\max} \approx 0.00116 \cdot \rho u_i^2 \qquad \text{if } u_i \geq 10 \text{ m/s} \tag{44}$$

when $D = 110$ mm.

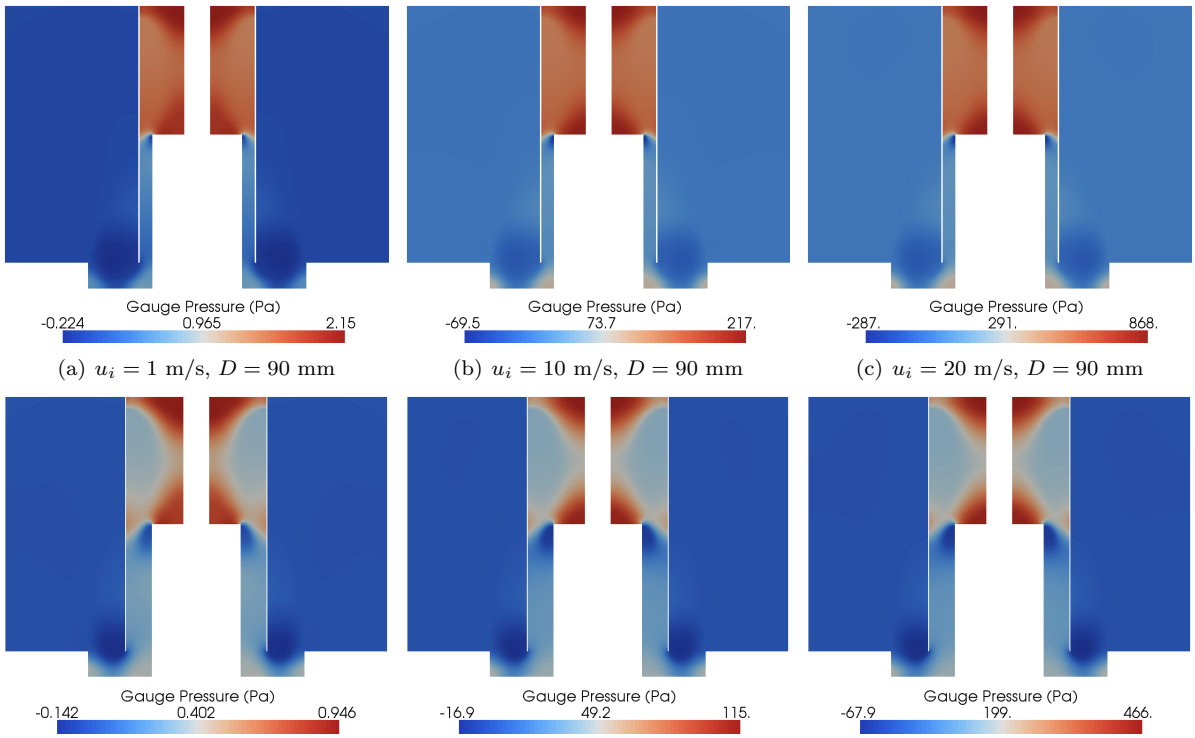

(a) $u_i = 1$ m/s, $D = 90$ mm (b) $u_i = 10$ m/s, $D = 90$ mm (c) $u_i = 20$ m/s, $D = 90$ mm

(d) $u_i = 1$ m/s, $D = 110$ mm (e) $u_i = 10$ m/s, $D = 110$ mm (f) $u_i = 20$ m/s, $D = 110$ mm

Figure 14: Pressure distribution as a function of input velocity u_i, and cap diameter D

The pressure trend along the falling zinc surface may be useful for modeling the chemical reactions, and are presented in Figures 15 and 16. The gauge pressure at the midpoint of the fall can estimated with

$$p_{\text{fall}} \approx 0.00025 \cdot \rho u_i^2 \qquad \text{if } u_i \geq 10 \text{ m/s} \tag{45}$$

when $D = 90$ mm, and

$$p_{\text{fall}} \approx 0.00030 \cdot \rho u_i^2 \qquad \text{if } u_i \geq 10 \text{ m/s} \tag{46}$$

when $D = 110$ mm. Eventually, it may be helpful to fit a general curve that would give the pressure all along the falling zinc surface.

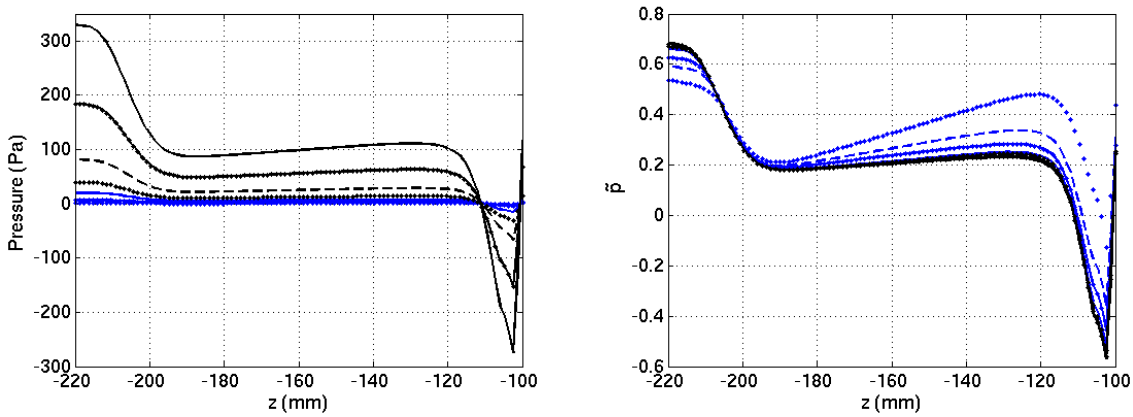

(a) Dimensional (b) Nondimensional

Figure 15: Pressure on the falling zinc surface, with cap diameter $D = 90$mm

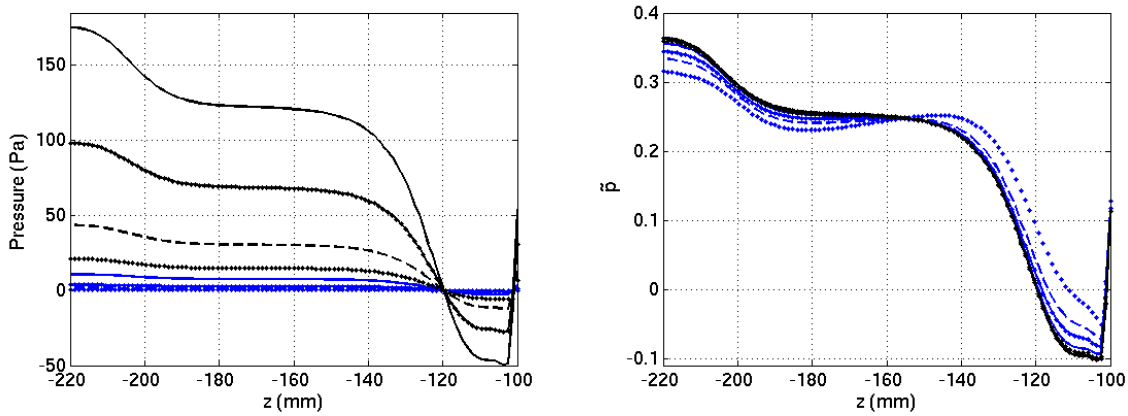

(a) Dimensional (b) Nondimensional

Figure 16: Pressure on the falling zinc surface, with cap diameter $D = 110$mm

In the dimensionless plots (Figures 15b and 16b), the varying balance between laminar and turbulent phenomena is again observed at the small velocities, which is why the previous estimates do not apply when $u_i < 10$ m/s. As before, the dimensionless curves for u_i <10 m/s are dispersed (Figure 15b and 16b).

The estimations provided in this section will be tested and refined once the apparatus is built. Once the uncertainties regarding the thermal parameters will be resolved, the resulting flow estimates will be used to model the dross formation reactions.

5 Conclusions

Preliminary computations demonstrate that a heat supply of 10 kW is sufficient to operate the zinc-flow apparatus within the industrially relevant ranges of the inlet flow rate. When the inlet velocity field is above 10 m/s, the flow behaviour surrounding the reaction zone is predictable, and may be extrapolated through the scaling of dimensionless numbers. For the 90 mm diameter cap, this corresponds to volumetric flow rates above 28 L/s; for the 110 mm diameter cap, this corresponds to flow rates above 35 L/s

Acknowledgements

This work has been funded by the *International Lead Zinc Research Organization*. The computations were performed at the *Industrial Materials Institute of the National Research Council of Canada* (IMI-NRC).

References

[1] F.Ajersch, F. Ilinca, and J.-F. Hétu, "Simulation of Flow in a Continuous Galvanizing Bath: Part I. Thermal Effects of Ingot Addition", *Metallurgical and Materials Transactions B*, vol. 35B, 2004, pp. 161-70.

[2] F.Ajersch, F. Ilinca, and J.-F. Hétu, "Simulation of Flow in a Continuous Galvanizing Bath: Part II. Transient Aluminum Distribution Resulting from Ingot Addition", *Metallurgical and Materials Transactions B*, vol. 35B, 2004, pp. 171-8.

[3] F. Ilinca, F.Ajersch, C. Baril and F.E. Goodwin, "Numerical simulation of the galvanization process during GA to GI transition", *International Journal for Numerical Methods in Fluids*, vol. 53, 2007, pp. 1629-46.

[4] F. Ilinca, J.-F. Hétu and F.Ajersch, "Three-dimensional numerical simulation of turbulent flow and heat transfer in a continuous galvanizing bath", *Numerical Heat Transfer A*, vol. 44, 2003, pp. 463-82.

[5] H. Balzer, S. Hölters; V. Sturm and R. Noll, "Systematic line selection for online coating thickness measurements of galvanised sheet steel using LIBS", *Analytical and Bioanalytical Chemistry*, vol. 385(2), 2006, pp. 234-9.

[6] D. Pitts and L. Sissom, "Property values of gases at atmospheric pressure", Appendix B of *Heat Transfer*, 2nd edition, Schaum's Outlines, McGraw-Hill (1988), p. 334.

[7] L. Ignat, D. Pelletier, F. Ilinca, "Adaptive computations of turbulent forced convection", *Numerical Heat Transfer A*, vol. 34, 1998, pp. 847-71.

[8] M.O. Deville, P.F. Fischer and E.H. Mund, "Dimensional Analysis and Reduced Equations", Section 1.7 of *High-Order Methods for Incompressible Fluid Flow*, Cambridge Monographs on Applied and Computational Mathematics, Cambridge University Press, Cambridge (2002), pp. 11-4.

[9] J.C. Tannehill, D. A. Anderson and R. H. Pletcher, "One-Equation Models", Subsection 5.4.5 of *Computational Fluid Mechanics and Heat Transfer*, Series in Computational and Physical Processes in Mechanics and Thermal Sciences, Hemisphere Publications, Philadelphia (1997), pp. 310-3.

[10] M.O. Deville, P.F. Fischer and E.H. Mund, "Solution Algorithms: Iterative and Newton Methods", Subsection 5.8.3 of *High-Order Methods for Incompressible Fluid Flow*, Cambridge Monographs on Applied and Computational Mathematics, Cambridge University Press, Cambridge (2002), pp. 277-8.

[11] B. E. Launder and D. B. Spalding, *Mathematical Models of Turbulence*, 6th ed., Academic Press, London (1972).